https://doi.org/10.1016/j.nanoen.2019.06.008

Mapping of Atomic Catalyst on Graphdiyne

Mingzi Sun[1], Tong Wu[1], Yurui Xue[2], Alan William Dougherty[3], Bolong Huang[*1], Yuliang Li[2] and Chun-Hua Yan[4]

1. *Department of Applied Biology and Chemical Technology, The Hong Kong Polytechnic University, Hong Hum, Kowloon, Hong Kong SAR, China.*
2. *Key Laboratory of Organic Solids, Institute of Chemistry, Chinese Academy of Sciences, Beijing 100190, PR China*
3. *Department of Computing, The Hong Kong Polytechnic University, Hong Hum, Kowloon, Hong Kong SAR, China.*
4. *Key Laboratory of Nonferrous Metal Chemistry and Resources Utilization of Gansu Province, State Key Laboratory of Applied Organic Chemistry and College of Chemistry and Chemical Engineering, Research Center of Biomedical Nanotechnology, Lanzhou University, Lanzhou, 730000, P. R. China*

*Email: bhuang@polyu.edu.hk

Abstract

Atomic catalysts as the frontier in atomic catalyst have attracted tremendous attention in recent electrocatalyst research. The performance of ACs strongly depends on the electronic interaction between the atoms and support. To supply a direct strategy for discovering more promising electrocatalysts, we propose a comprehensive mapping study of anchoring transition metals on the graphdiyne (GDY). The electron transfer ability and zero-valence stability are quantified based on the redox process between surface metal and GDY support. The different electron transfer number and directions between the transition metals and GDY are also compared, in which the initial one-electron transfer is the most difficult. Among all the TMs, Co, Pd and Pt have displayed exceptional stability of zero-valence catalyst based on the evident energy barrier difference between losing electrons and gaining electrons. Experimental results support the remarkable performance of our screened candidates, which have opened a new possibility to achieve novel high-performance zero-valence ACs. Moreover, we outlook the introduction of the deep-learning algorithm in the future advanced mapping strategy for achieving more complicated ACs. This work not only supplies innovative electrocatalyst candidates but also exhibited an innovative approach for studying the electrocatalysts that can further apply to more material systems.

Introduction

Particle size is one of the most significant factors that determine the performance of a catalyst [1-3]. Downsizing the particles not only improves the surface-area-to-volume ratio but also results in more complexed changes in both physical properties and chemical properties. The currently predominant metal catalysts prepared in nano-size with fine dispersion have reached a remarkable catalysis activity in practical applications [4-8]. In this case, only a small portion of the metals that are exposed to the surface is involved in the reaction, and the active sites on the surface might be multi-functional, which causes the reduction of selectivity. Therefore, to reach the maximum utilization of the specific active site, and to improve the efficiency of metal nanoparticles, the particle size of the metal atoms should be further reduced. Hence, the ultimate reduction of particle size leads to the atomic catalyst (AC). This approach features atomically dispersed metal atoms without neighbouring interaction as active centres with 100 % utilization efficiency. The significant difference in particle size results in the increasing of surface free energy of metal components. Such a highly active and efficient catalyst was introduced in 2001 of CO oxidation [9]. The activity of AC is mainly controlled by its unique geometries, the subsequent electronic effects, and the strong interaction with the support. The single metal atom can be anchored on the surface by adsorption and doping process, in which the adsorption is less energetically unfavourable due to the weak bonding with the surface. Since the active sites of AC are ascribed to the well-distributed single metal atom, the possible catalytic pathways are relatively fixed. This is distinct from conventional nanoparticle catalysts that varied active sites generate different possible catalytic pathways. Attributing to the minimization of metal ensembles, the catalytic selectivity of ACs are significantly enhanced. For instance, the AC of Pt supported on TiN has been reported that is strongly selective towards the two-electron pathway in oxygen reduction reactions (ORR) and the direct dehydrogenation in formic acid oxidation rather than methanol oxidation [10]. Therefore, it is worthy to note that AC is not definitely superior to conventional nano-size materials. The isolated metal atoms in AC also exhibit different electronic properties from those of nano-size metal catalysts. Instead of interaction with neighbouring metal atoms, the single metal atoms display strong interaction with the support based on active charge transfer. The direction and the intensity of the charge transfer can be determined by the chemical potentials of the metal atoms and support.

As a consequence of charge transfer, the valence state of AC has attracted intense attention in recent years. Previously, in nano-sized materials, the valence states of the metal components usually exhibited mixed with multiple valence states, which largely induce the difficulties to distinguish the catalytic role of each valence state [11]. This problem is easily solved in single atom AC as the dispersed metal atoms are in the same coordination environment and hence in the same valence states. The valence state of the AC is highly correlated to the catalytic performance. If the valence state of the metal atoms can be efficiently adjusted by different supporting material or the coordination environment, AC would be a useful tool for the investigation of the correlation between metal valence states and catalytic performances. Meanwhile, the strong interaction with support also means the properties of support could be modified by the anchored metal atom. The support material can be stabilized to prevent degradation of the catalyst, or it can be induced to form defects on the supporting material by the metal atom. For instance, the strongly-pinned La atoms on the γ-Al_2O_3 inhibit both sintering and the transformation of support [12]. The noble metal atoms on reducible supports (Pt/FeO_x, Ir/CeO_2, etc.) are found to activate the lattice oxygen on the surface [13-17]. Compared to pure metal atoms, the ACs are advantageous for their remarkably improved stability. The stability is also due to the strong interaction with the support. In most reported systems, the positively charged AC are observed in Pt_1/FeO_x catalysts [18], Co-C-N complex bonded carbon fiber [19] and Cu-N-C nanosheets [20]. In contrast, the zero-valence catalyst is

a novel concept that currently developed closely related to AC. For instance, in the prevailing M-N-C system (M=metal, N=nitrogen, C=graphene, metal atoms are distributed on the nitrogen-doped graphene sheet), it has been observed that the sp-d orbital-charge transfer can passivate the open-shell d^8 Fe and Ni to inert closed-shell d^{10} configuration, as experimental results show the Ni and Fe in M-N-C system are in their metallic state [21-22]. Moreover, other reported zero-valence catalysts, such as Ni-, Fe- and Pd-GDY [21, 23] and Ni-doped-nanoporous graphene [24] are all also prepared as single atom AC, which has shown great catalytic activity in experiments. The zero-valence have been achieved through the strong electronic metal-support interaction as well as the maximum surface-to-volume-ratio of the single-atomic catalyst makes full utilization of the active site.

However, the significance of preparing a zero-valence catalyst is vague because the catalytic activity cannot be simply explained by the valence state of the active site. Instead, the electronic interaction between the atoms and support which modifies the electronic structure of the active site is considered as the origin of the enhanced activity. The zero-valence state reported by experimental analysis results should be ascribed to the charge compensation aroused from the metal atom-support interaction [21]. In other words, the zero-valence state is the subsequent observations of the atom-support interaction, but not the origin of the catalytic activity. As a two-dimensional carbon material, GDY possesses abundant uniform pores, high stability with strong reduction ability that has been reported in many applications [25-27]. Thus, GDY has become ideal support for the AC that shown exceptional catalytic reactivity. More importantly, for these zero-valence catalysts, it is very interesting to discover that the nearby active sites are activated by the anchoring metal [21, 23, 28]. In the works by Li *et al.*, an extraordinary HER catalyst has been fabricated based on Ni-, Fe-doped GDY with ultra-low onset overpotential as well as the long-term stability [21]. The active sites are located on but the neighbouring carbon atoms due to the *sp-d* charge transfer between the doped metal atoms and GDY support. A similar phenomenon also found in the sulfur atoms on single-Pt-doped MoS_2 for H adsorption [28]. Therefore, the interaction results between the introduced single atom and the support indeed dominate the electrocatalytic rather than the single-atom or the support itself.

Zero-valence catalyst is a frontier in heterogeneous ACs. To realize more promising zero-valence catalyst, here we present a mapping strategy based on transition metal (TM)-GDY systems, in which the charge transport and stability has been well analyzed and screened. This work will excavate more possible catalysts based on theoretical calculations, which substantially accelerates the development of GDY. Moreover, this mapping strategy can supply a more accurate and general description of the charge transport that can be extended to other AC systems or even complex composite catalysts for further screening of unknown catalyst with high catalytic selectivity and activity.

Results and Discussion

Theoretical Mappings

A good AC should always be equipped with high electron transfer ability, which means the similar ability of fast electrons obtaining and transferring out electrons. Since the GDY has shown great potential as TM host to achieve stable AC with the zero-valence state, more promising candidates are highly desired for the broad applications in electrocatalyst. By considering the electron transfer ability through simple redox reactions, we have applied such strategy to 26 TMs from IIIB to IB of 3d to 5d electronic configurations in the periodic table.

To screen out more potential TMs that can be anchored on the GDY with the zero valence, the redox reactions are as follows:

$$\begin{cases} Oxidation: \ \mathrm{M^{2+}} + 2\mathrm{GDY^{0}} \rightarrow \mathrm{M^{0}} + 2\mathrm{GDY^{+}} \\ Reduction: \ \mathrm{M^{0}} + 2\mathrm{GDY^{0}} \rightarrow \mathrm{M^{2+}} + 2\mathrm{GDY^{-}} \end{cases} \quad (1)$$

$$\text{Overall: } 4\mathrm{GDY^{0}} \rightarrow 2\mathrm{GDY^{+}} + 2\mathrm{GDY^{-}} \quad (2)$$

The electron transfer of the whole TM-GDY systems are classified into the oxidation and reduction reactions. To simplify and unite the mapping, we firstly consider the valence of all the metals as +2. By comparing the barriers of both reaction trends, we can derive the zero-valence stability of transition metal on GDY and their overall electron transfer ability. The high barrier of the oxidation reaction indicates the transition metal remain high valence with a strong hinder to return to the zero valence. On the contrary, the high barrier of reduction energy leads to a stable zero-valence state of TM on GDY due to the difficulties of losing electrons. The calculated the redox energies of TMs from 3d to 5d are based on applying DFT calculations to Eq. (1) and Eq. (2), where the length of the column represents the scale of barriers (**Figure 1a-1c**). Notably, the majority of reduction reactions dominate the overall trend due to the evidently larger barriers than that of the oxidations. Besides the reported Ni, Fe as successful zero valence catalyst on the GDY [21], Ti and Co exhibit higher zero-valence stability due to the even higher reduction reaction barriers. Among the 4d TM, the results of Pd support their anchoring potential as an exceptional catalyst on the GDY surface. Tc and Cd are unexpected candidates that shows even slightly higher redox barrier than that of Fe. However, only Rh in all the TM shows a converse trend that the oxidation reaction dominates the redox trend, indicating the preference in preserving the oxidation states. The overall anchoring stability of 5d TM is slightly weaker than 3d and 4d TM. Beyond the well-known catalyst, Ir, Hg and Re displays very strong trend in stable zero valence trend, in which Hg shows even better performance than Pt. Interestingly, we also found out that the commonly used noble metal catalysts Au, Ag and Cu did not exhibit any advantages in stabilizing the zero-valence on the GDY surface. The detailed comparison of the oxidation and reduction energy with the pristine GDY surfaces are also presented (**Figure 1d-1f**). The pure GDY surface shows high barriers for both gaining electrons and losing electrons, in which the reduction reaction is slightly favorable. With anchoring TMs, the electron transfer ability has been largely enhanced due to the lowering of redox barriers, meaning a higher catalytic reactivity. In the detailed discussion, the superior zero-valence stability of Co is attributed to the tremendously small barrier of oxidation reaction to recover to zero-valence, which has become the best anchoring choice for achieving zero-valence ACs on the GDY. Similarly, Pd and Tc also display stronger zero-valence state trend due to the low barrier of oxidation reactions. The barrier variations of redox reactions of 5d TM are not as evident as 3d and 4d TM, in which both oxidation and reduction barriers are slightly smaller. In general, the reduction trend is in accordance with the total energy trend, suggesting the dominant role in the controlling of the redox (**Figure 1g-1i**). The distinct behaviour of Rh endows it with the strong electron donating ability with stable oxidation states, demonstrating a great potential electrocatalyst for ORR, NRR electrocatalysis.

To further align the redox with the element, we have plotted the dependence of the total energy on the number of d orbital electrons (**Figure 2a**). Except the abnormal Ti and Pd, all the element with electronic configuration less than d^4 or d^{10} has a relatively close total energy barrier for the redox (~0.75 eV), suggesting lower stability of remaining zero valence on the GDY. For all the electronic configuration between d^6-d^9, the redox energy barrier has increased to over 1 eV, which includes most of the potential candidates for achieving stable zero valence on GDY.

By comparing the total energy from the periodic table arrangement, the energy difference becomes more apparent (**Figure 2b-2d)**. Clearly, the total energy suddenly increases from group VIIB to group VIII, which also shows the abnormally low energy barriers. For those metal with high reduction barrier, they usually exhibit relatively low barriers in oxidation energy that support their good stability as zero-valence. Particularly, Hg and Rh can represent the extreme conditions, one is stably anchoring as zero valence state catalyst while the other is remaining oxidation state easily. By utilizing the subtle difference of sensitivity to the redox after anchoring on GDY, more precise control of the catalysts can be further realized by the careful combination of elements of anchoring by the screening.

Since the redox process model considers the transition metal directly become stable +2 oxidation state, the initial situation of losing one electron of transition metal should also be studied for comparison (**Figure 3a-3c**). The redox reactions are based on follows,

$$\begin{cases} \text{Oxidation}: \ \mathrm{M^{+} + GDY^{0} \rightarrow M^{0} + GDY^{+}} \\ \text{Reduction}: \ \mathrm{M^{0} + GDY^{0} \rightarrow M^{+} + GDY^{-}} \end{cases} \tag{3}$$

$$\text{Overall: } \mathrm{2GDY^{0} \rightarrow GDY^{+} + GDY^{-}} \tag{4}$$

In contrast with the original reactions Eq. (1)- (2), the energy barriers of both reduction and oxidation reaction are evidently enlarged to over 2 eV, suggesting the initiation of electron transfer is difficult. Moreover, the scales of total energy barrier have been significantly alleviated due to the oxidation reactions barrier increases to similar to that of the reduction reaction. This phenomenon demonstrates a much more inert electron transfer behavior on the GDY. The total energy barrier displays a similar trend as Eq. (1)- (2), in which Rh is still distinct with all the other TM, supporting their reduction ability. The advantages of Ti, Co, Re and Hg become subtle when compared with other metals. Thus, it is concluded that the TMs prefer staying at the redox between higher oxidation states and zero valence on the GDY.

For many alloy catalysts, metals usually mediate in donating electrons and receiving electrons to accelerate electron transfer for the electrocatalysis. Therefore, another redox reaction direction is calculated as reactions shown below (**Figure 3d-3f**),

$$\begin{cases} \mathit{Oxidation}: \ \mathrm{M^{0} + 2GDY^{0} \rightarrow M^{2-} + 2GDY^{+}} \\ \mathit{Reduction}: \ \mathrm{M^{2-} + 2GDY^{0} \rightarrow M^{0} + 2GDY^{-}} \end{cases} \tag{5}$$

The overall reaction trends are similar to the previous electron lose direction as Eq. (1) but the total energies have been lowered. In details, we observe some different behaviors. For example, the negative reduction reaction barrier for Ti has led to a high total energy barrier. A similar situation can be found in Ir as well. These suggest that the low ability to preserve electrons in both Ti and Ir, which immediately recover to zero valence states. In contrast, the high barrier of total redox reactions for Co can be attributed to the hinder of receiving electrons on GDY. The total energy barriers of 4d TM are determined by the reduction reaction barriers as the previous strategy. To further confirm the electron-affinity of all the TM, we have plotted the linear correlation between the total energy of the TM-GDY system and the valence change from -2 to +2. The intercept of the linear fitting demonstrates the scale of negative correlation energy for the element (**Figure 3g**). The larger the intercept, the more electron-affinitive. The electron-affinity shows undulate from 3d to 5d TM. In 3d TM, Co and Ni show high electron-affinity while Ti becomes not active in electron-affinity that is consistent with the low ability to preserve electrons in **Figure 3d**. In 4d, Pd ranked the highest electron-affinity, supporting

the previous research [29]. Unexpectedly, Os shows the highest electron-affinity among all the TM, even higher than Pt. The low electron-affinity of Ir can be ascribed to the same reason as Ti. Overall, we can roughly screen out the Re, Tc, Os, Co, Pd, Pt, Ni and Hg as the most electron-affinitive elements. The linear slope of the TM-GDY system represents the possibility of stability, which is also pivotal to the electrocatalyst. By the combination with the electron-affinity, the most stable TM-GDY with rich electron are Co, Pd, Ni, Ir and Pt.

Besides the normal TM, we should also extend our strategy to more elements such as lanthanide series, which has been proven with high catalytic reactivity as well [30-31]. However, lanthanide usually displays the stable non-zero valence states, which is difficult to realize the zero-valence as TMs. Therefore, we investigate the anchoring condition of lanthanide (Ln = La-Yb) on the GDY of their common oxidation valence states as following reactions.

$$\begin{cases} \text{Oxidation}: \ \mathrm{Ln^{3+} + GDY^{0} \rightarrow M^{2+} + GDY^{+}} \\ \text{Reduction}: \ \mathrm{M^{2+} + GDY^{0} \rightarrow M^{3+} + GDY^{-}} \end{cases} \tag{6}$$

The only exceptional valence state (+3/+4) is applied to Ce since the +2 valence state is not stable. As shown in **Figure 3h**, a fluctuation of the energy barrier has been noted, representing the large difference between elements with less regulation than the TMs. Extremely different behaviors are noted rather than a general trend that is applicable to most elements. The completely two opposite trends are summarized before and after Eu. From La-Eu, the reduction reactions dominate the total energy with much larger energy barriers than the oxidation reactions, meaning the higher preference of +2 valence state than the +3 valence state. However, the sudden turnover trend initiates from Gd, the oxidation reactions show much larger energy barriers, which lead to the +3 oxidation states of the anchoring lanthanide metals on the surface. Interestingly, the Tm becomes +2 valence preference while the Yb shows no preference with low energy barrier of both redox processes.

To better screening out the potential candidates for stable anchoring on GDY as efficient catalysts, a systematic summary on the electron transfer ability evolution has been demonstrated (**Figure 4a**). The electron transfer ability has been calculated based on the following reactions Eq. (7)- (8).

$$\begin{cases} \text{Lose electons}: \ \mathrm{M^{0} + GDY^{0} \rightarrow M^{+} + GDY^{-}} \\ \text{Gain electrons}: \ \mathrm{M^{0} + GDY^{0} \rightarrow M^{-} + GDY^{+}} \end{cases} \tag{7}$$

$$\begin{cases} \text{Lose electons}: \ \mathrm{M^{0} + 2GDY^{0} \rightarrow M^{2+} + 2GDY^{-}} \\ \text{Gain electrons}: \ \mathrm{M^{0} + 2GDY^{0} \rightarrow M^{2-} + 2GDY^{+}} \end{cases} \tag{8}$$

Though metals usually exhibit electron lose preference, most metals show a lower energy barrier in obtaining electrons on GDY. For instance, Pd with $4d^{10}$ exhibits the possibility of obtaining extra active electrons that can lead to the formation of electron-affinitive $4d^{10+\delta}$, which can break the hinder for electron supply for the adsorption in electrocatalysis. Therefore, Pd, Co, Pt should all display relatively stronger electron gaining ability than the other TMs. Ti has shown the lowest electron gaining ability, but the low barrier of oxidation results in the quick loss of electrons as well. Rh is the only exceptional metal with the preference of losing electrons, which remains the normal metal properties on GDY. As the electron transfer increases to two electrons, we observe the overall reduction on the energy barriers for both

electron loss and gain. This indicates that the anchoring on GDY has enhanced the electron transfer ability of TM. In **Figure 4b**, we have plotted the contour mapping to demonstrate the energy barrier change during the charge transfer. We can observe the color changes from mostly red to green, representing the energy decrease trend. Moreover, we calculated the energy difference between losing electrons and gaining electrons to illustrate the charge transfer preference of TMs in a direct way (**Figure 4c**). It is noted that the promising candidates Pd, Co, Pt and Hg showed a strong reduction trend at large electron transfer while remaining stable the zero-valence at the initial charge transfer. Especially, the nearly equivalent energy barriers for electron loss and gain in the promising TMs suggests the higher anchoring possibilities of zero-valence state. Interestingly, Ti evidently changes from oxidation trend to the reduction trend when the electron transfer number increases, which demonstrates lower stability for undertaking electron transfer as electrocatalysis. Due to the strong toxicity of Hg, Pd, Co and Pt display the most stable anchoring conditions at initial charge transfer and electron-rich for strong electron transfer during the electrocatalysis as the promising choices.

To further investigate the interaction between the metal and the support in the GDY-M electrocatalysts, the real-space HOMO and LUMO contour plots and the simulated electron energy-loss near-edge structure (ELNES) calculation of selected metals including the best candidates (Pd, Pt, Co, Ir) and the reported candidates (Fe, Ni) have been carried out. As we can see, the evident charge density distribution has been observed in GDY-Pd, GDY-Co and GDY-Ir induced by the stabilized zero valence state of the metals (**Figure 5a**). This phenomenon is highly consistent with the previously reported GDY-Ni, indicating the guarantee of the fast exchange for HER electrocatalysis [21]. Interestingly, the GDY-Co shows the high electroactivity based on the strongest interaction with the GDY support, suggesting a potential electrocatalyst candidate for reduction reaction process.

Experimental Comparison

To verify the screened electrocatalyst, we have compared one of the best candidates GDY-Pd with GDY-Fe and GDY-Ni, in which GDY-Fe and GDY-Ni should show less competitive performance than GDY-Pd as we predicted by the mapping results. The corresponding experimental of GDY-Ni, GDY-Fe and GDY-Pd are synthesized and tested to verify the validity of our calculations. Sub-ångström-resolution, aberration-corrected scanning transmission electron microscopy (STEM) was employed to characterize the configuration and dispersion of metal atoms on GDY. Examination of various regions of the catalysts revealed the only presence of singly anchored Ni atoms **(Figure S1a-c)**, Fe atoms **(Figure S1d-f)**, and Pd atoms **(Figure 1g-i)** on GDY. X-ray absorption near-edge structure (XANES) and extended x-ray absorption fine structure (EXAFS) spectra were performed to confirm that only atomically anchored metal atoms on GDY. For GDY-Fe **(Figure S2a)**, there was only one notable peak at ~ 1.5 Å from the Fe~C contribution and no Fe-Fe contribution (at ~ 2.2 Å) was observed, confirming the only presence of singly dispersed Fe atoms in the catalyst. For GDY-Ni **(Figure S2b)**, there was only one notable peak at ~ 1.6 Å from the Ni~C contribution and no peak in the region 2 to 3 Å from the Ni-Ni contribution, confirming that Ni exists predominantly as isolated atoms. The EXAFS spectrum of GDY-Pd **(Figure S2c)** featured a peak ~1.5 Å, less than Pd–Pd contribution (ca. 2.5 Å), confirming the Pd exists predominantly as isolated atoms.

The simulated K-edge and L-edge of the reported electrocatalysts are shown in **Figure 5b**. The experimental derivative XANES spectra indicate that the GDY-Fe **(Figure S2d)**, GDY-Ni **(Figure S2e)**, and GDY-Pd **(Figure S2f)** mainly consist of Fe(0), Ni(0), and Pd(0) atoms,

respectively. Our simulated spectra show a good agreement with the main peak marked in the experimental results, demonstrating the stabilization of zero-valence. Moreover, the other simulated spectra in GDY-Co, GDY-Pt and GDY-Ir also display a similar position of the main peak in the pristine metal XANES results.

Then we move to the electroactivity characterization of the as-prepared GDY-M electrocatalysts. GDY-Pd, GDY-Fe, and GDY-Ni -possess high catalytic activities with the small onset overpotentials close to that of commercial Pt/C **(Figure S3a-3b)**. To deliver the current density of 10 mA cm^{-2}, GDY-Pd needs the smaller overpotential of 55 mV than that of GDY-Fe (66 mV), GDY-Ni (88 mV), GDF (578 mV) and CC (642 mV) (**Figure S3c, Table S1**). These values are also more favourable than the other earth-abundant HER electrocatalysts (**Table S1**). Turnover frequency (TOF) is an important criterion when evaluating the authentic activities of catalysts having various mass loadings. GDY-Pd has a large TOF value of 16.7 s^{-1}, which is also higher than GDY-Fe (4.15 s^{-1}), GDY-Ni (1.59 s^{-1}), Pt/C (11.5 s^{-1}) [32], Pt-GT (7.22 s^{-1}) [33], and conventional single-atom catalysts, including $Mo_1N_1C_2$ (0.262 s^{-1}) [34] and Co-NG (0.101 s^{-1}) [35]. Thus, the preliminary experimental results have confirmed the feasibility of the screen metal for anchoring on the GDY, supporting the potential in other unreported candidates as well.

Outlook with AI Technology

The verification of this work is a good start-up reference for future work in this area. In the future, the introduction of AI-driven and big data technologies will be of great significance in accelerating the screening efficiency and accuracy in the more complicated systems (**Figure 6a).** In recent years, the rapid development of artificial intelligence-based machine learning techniques such as deep-learning has achieved important advances not only in those in mainstream artificial-intelligence research but also in physical and chemical science by the adoption of these approaches [36-42]. Most excitedly, with deep learning, given enough data and sufficient domain knowledge, the appropriate screening strategy is able to determine all known physical laws as well as those currently unknown by uncovering the hidden latent information within the data. Leveraging on the theoretical calculation database, we can further apply the multi-functional parameters including redox barrier (a), electron-affinity (b), stability (c), electronegativity (d) and electronic configurations (e) etc. as follows,

$$\begin{cases} \boldsymbol{f = g\ (a, b, c, d, e\ \ldots\ldots)} \\ \boldsymbol{g = g_{ele}\ (a', b', c', d', e'\ \ldots\ldots)} \end{cases} \quad (\mathbf{9})$$

Then we introduce possible algorithm in machine-learning to classify the complex database and screen out the potential candidates. The Fuzzy C-Means (FCM) algorithm has a strong ability to classify a data-set into groups based on data-clustering, whilst maintaining any inherent uncertainty between these groups (**Figure 6b**). Furthermore, the nature of the FCM algorithm is such that it assumes we do not have much knowledge about the structure of the classes themselves. The FCM algorithm is an unsupervised learning method, one must at least decide the number of clusters which should be found, but henceforth FCM form the cluster groups automatically. The optimisation objective function of the standard FCM algorithm $J = \sum_{i=1}^{N}\sum_{j=1}^{M} u_{i,j}^{p}\left\|x_i - c_j\right\|^2$ has an important uncertainty term $u_{i,j}^{p}$ which is known as the membership function.

$$J_{SAFCM} = \sum_{i=1}^{N}\sum_{j=1}^{M}\sum_{k=1}^{\Omega} u_{k|i,j}^{p}\left\|\eta_{i,j}c_k\right\|^2 + \lambda\sum_{i=1}^{N}\sum_{j=1}^{M}(\eta_{i,j} - \Gamma(\eta_{i,j}))^2 \quad (10)$$

For any given input data x, there exists a corresponding membership value which denotes the certainty that the data-point x belongs to some particular class. Additionally, one must note that the FCM algorithm works much like other clustering algorithms, such that, it forms classes by looking at a particular distance metric between the data points and the class-cluster mean. The class cluster Mean in $J = \sum_{i=1}^{N}\sum_{j=1}^{M} u_{i,j}^{p}\left\|x_i - c_j\right\|^2$ is denoted by c, and the distance between the data-point and the mean is often found using distance metrics such as the Euclidean distance. Some data-sets may correlate with one another or have a higher probability that they belong to a particular class depending on the density of similar value datum 'locally' to it [43]. Eq. (10) shows a modified FCM algorithm which considers this spatial relationship between the data-points, $\eta_{i,j}$ is a local image pixel-gain term which biases a certain data-points likelihood to belonging to a cluster based on the amount of other similar-valued pixels which exist locally to it. An additional term Γ , which is a filter response around a local area of any data-point x, is also added to the equation for Lagrangian optimisation of $\eta_{i,j}$.

To further enhance results, if a data-set has some clusters which are not easily linearly separable such as those shown in **Figure 6c**, we can further develop a machine learning algorithm to utilise Kernel functions. Essentially, the kernel function is a mapping function which can take any n-dimensional data-set and map it to a higher N-dimensional one to allow for easier separation; this is demonstrated visually in **Figure 6c**. In the case of the FCM, by combining the ability of Kernel function with its ability to model uncertainties within data-sets, we can significantly increase the likelihood of correctly classifying a data-set which has unusually distributed and overlapping features. One such example of a Kernel-based version of Eq. (10) is shown in Eq. (11), where K is the radial basis function Kernel [43].

$$J_{KAFCM} = \sum_{i=1}^{N}\sum_{j=1}^{M}\sum_{k=1}^{\Omega} u_{k|i,j}^{p}\,(1 - K(x_i, \eta_{i,j}c_k)) + \lambda\sum_{i=1}^{N}\sum_{j=1}^{M}\left(1 - K\left(\eta_{i,j}, \eta_{i,j}D_{i\in\phi}\right)\right) \tag{3}$$

The single-metal ACs is the initial step for the great potential of GDY-based electrocatalysts. To achieve the rational design with expected multi-function electrocatalyst, the multi-atoms and multi-metals composite ACs are the future research directions (**Figure 6d**). Considering the structural complexity and the interaction between metal atoms, we further introduce the configuration entropy into the multifunctional architecture Eq. (4) for deep-learning driven screening in ACs with the more precise prediction of thermodynamic, physiochemical properties to achieve the converse design and modifications of GDY-based electrocatalysts.

$$\begin{cases} \boldsymbol{S = k_B ln\, W} \\ \boldsymbol{W = \prod(W_i + W_j + W_k)} \\ \boldsymbol{\Delta G = -T\Delta S = -k_B T ln\left(\prod \frac{W_i' + W_j' + W_k'}{W_i + W_j + W_k}\right)} \end{cases} \tag{4}$$

Conclusion

In summary, GDY-based ACs with potentially superior performance are identified by the proposed mapping strategy. By considering the electron transfer ability as the redox process, we systematically studied the possibility of anchoring on GDY as exceptional ACs of all the TMs (IIIB to IIB) as well as the lanthanide elements. The feasible charge transfer redox models evaluated the GDY-based electrocatalysts from an innovative perspective. Beyond the present

reported Fe, Ni and Pd, our strategy proposed Co and Pt as available choices for achieving high-performance and stable ACs. Additional experimental results also strongly support the validity of our strategy. The introductions of advanced deep-learning algorithm and big-data technologies demonstrate a new direction of rational designs and modifications for complicated ACs with expected performance. This start-up work supplies a general strategy in dealing with complicated electrocatalysis process that not only benefits the GDY-based ACs but also other electrocatalysts.

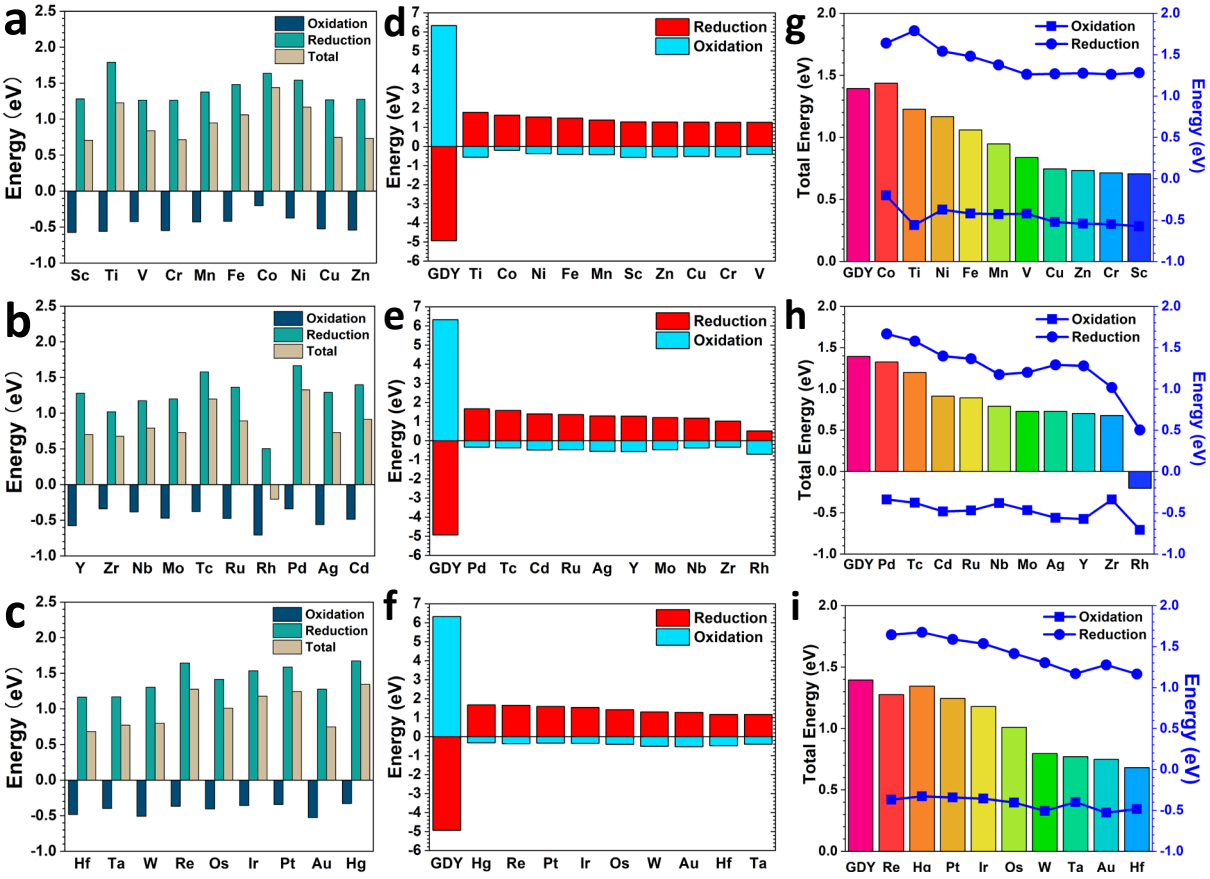

Figure 1. Energy mapping of redox reactions for TM-GDY. (a)-(c) Summary of redox of 3d, 4d and 5d TM. (d)-(f) The comparison of oxidation and reduction reactions between GDY and 3d, 4d and 5d TM. (g)-(i) The effect of reduction and oxidation reactions to the overall redox trend of 3d, 4d and 5d TM.

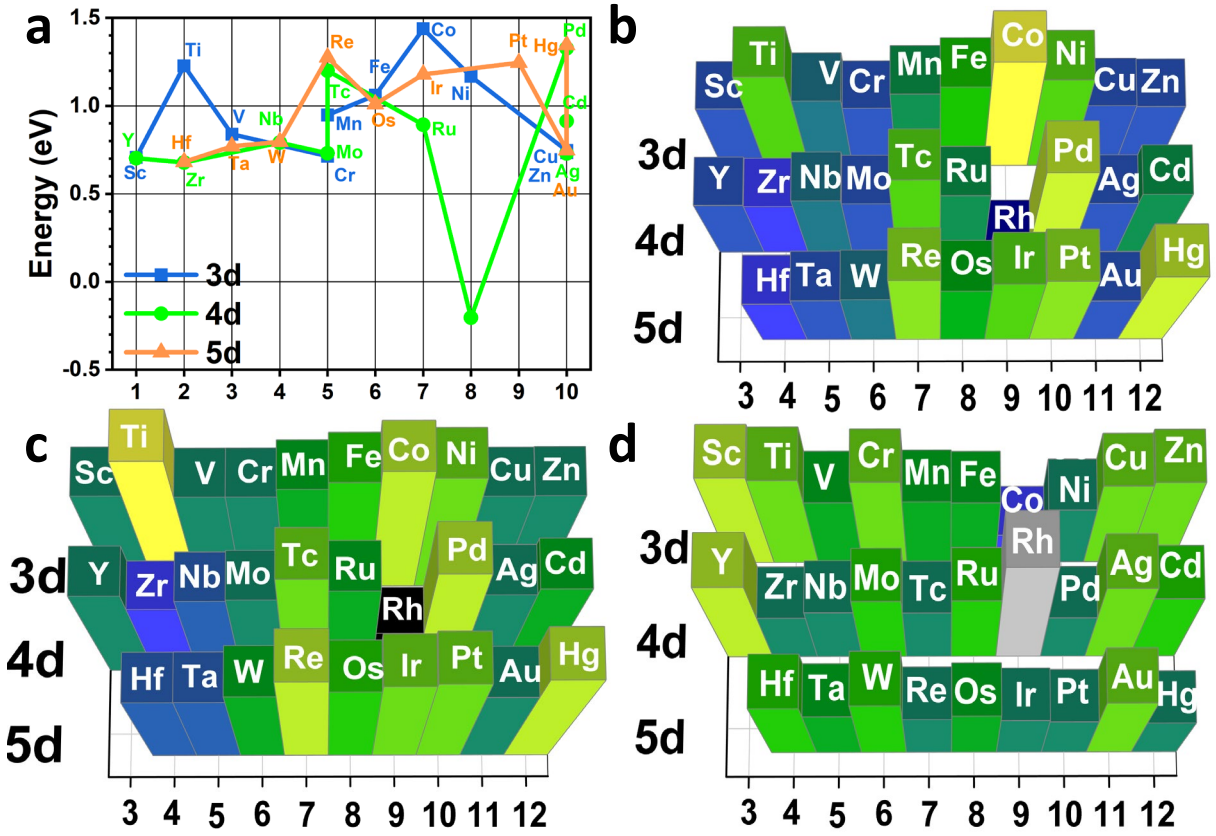

Figure 2. The overall anchoring ability of TM-GDY. (a) The dependence of anchoring ability of TM on electrons of d orbitals. (b) The mapping of zero-valence anchoring ability of TM in periodic tables. The decomposition of the mapping into (c) oxidation and (d) reduction reactions.

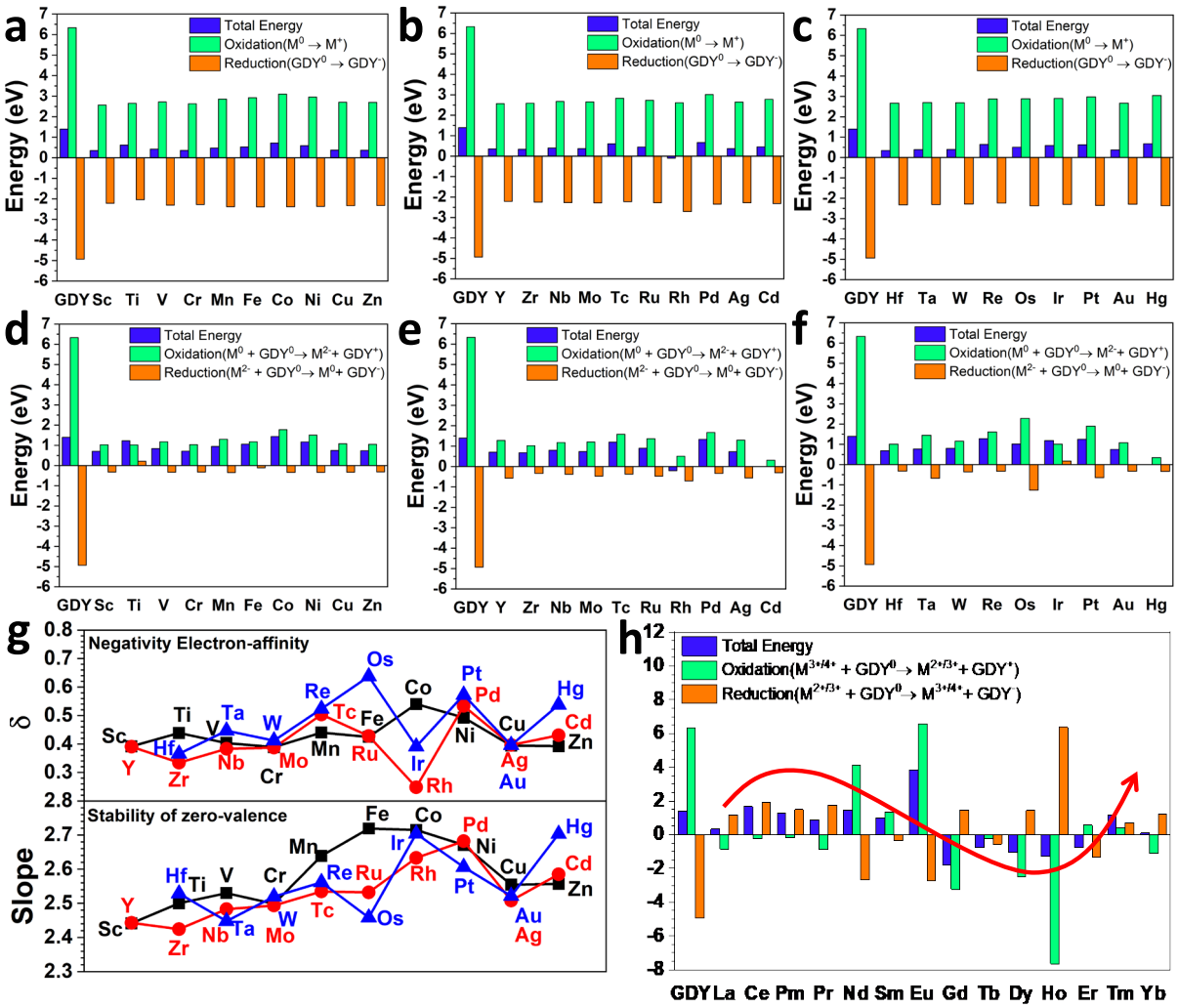

Figure 3. (a)-(c) The mapping of the interaction between GDY and 3d, 4d and 5d TM. (d)-(f) Another energy mapping strategy of redox reactions for 3d, 4d and 5d TM-GDY. (g) The mapping of negativity electron-affinity and stability of zero valences TM-GDY. (h) Redox reactions mapping of lanthanide ions on GDY.

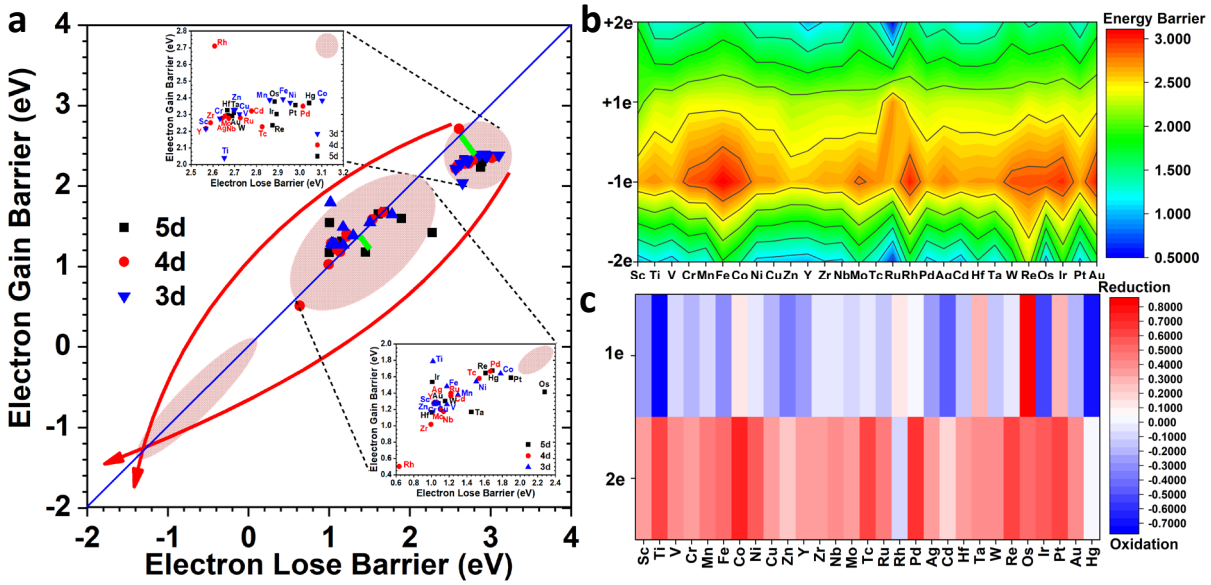

Figure 4. (a) Illustration of the evolution of electron transfer of TM-GDY. (b) Mapping of the electron transfer ability of metal on GDY. (c) Mapping of the electron transfer stability on GDY.

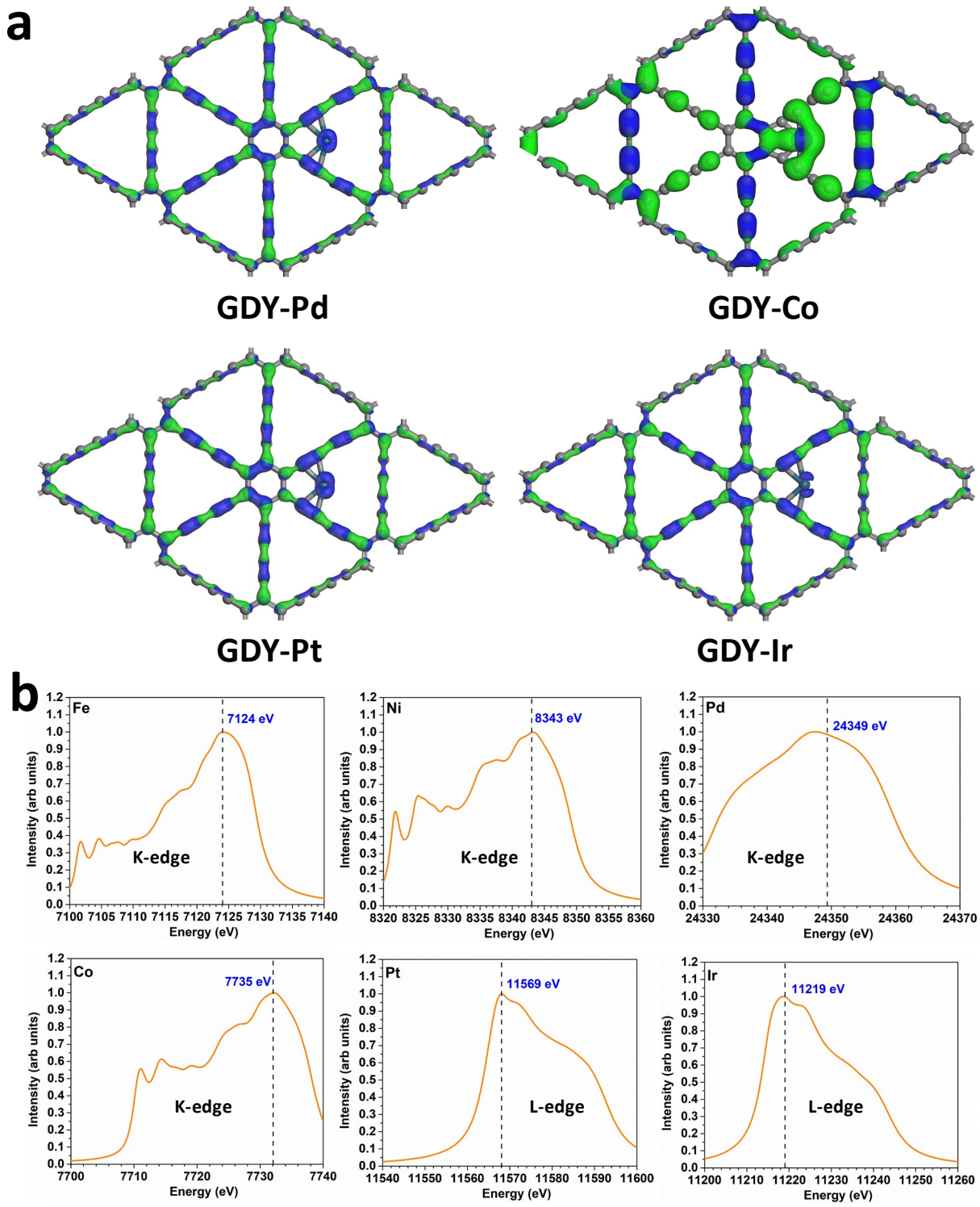

Figure 5. (a). The real-space HOMO and LUMO contour plots on the screened candidates of GDY-M electrocatalysts. (b) The simulated K-edge and L-edge of the reported GDM-M and screened GDY-M electrocatalysts.

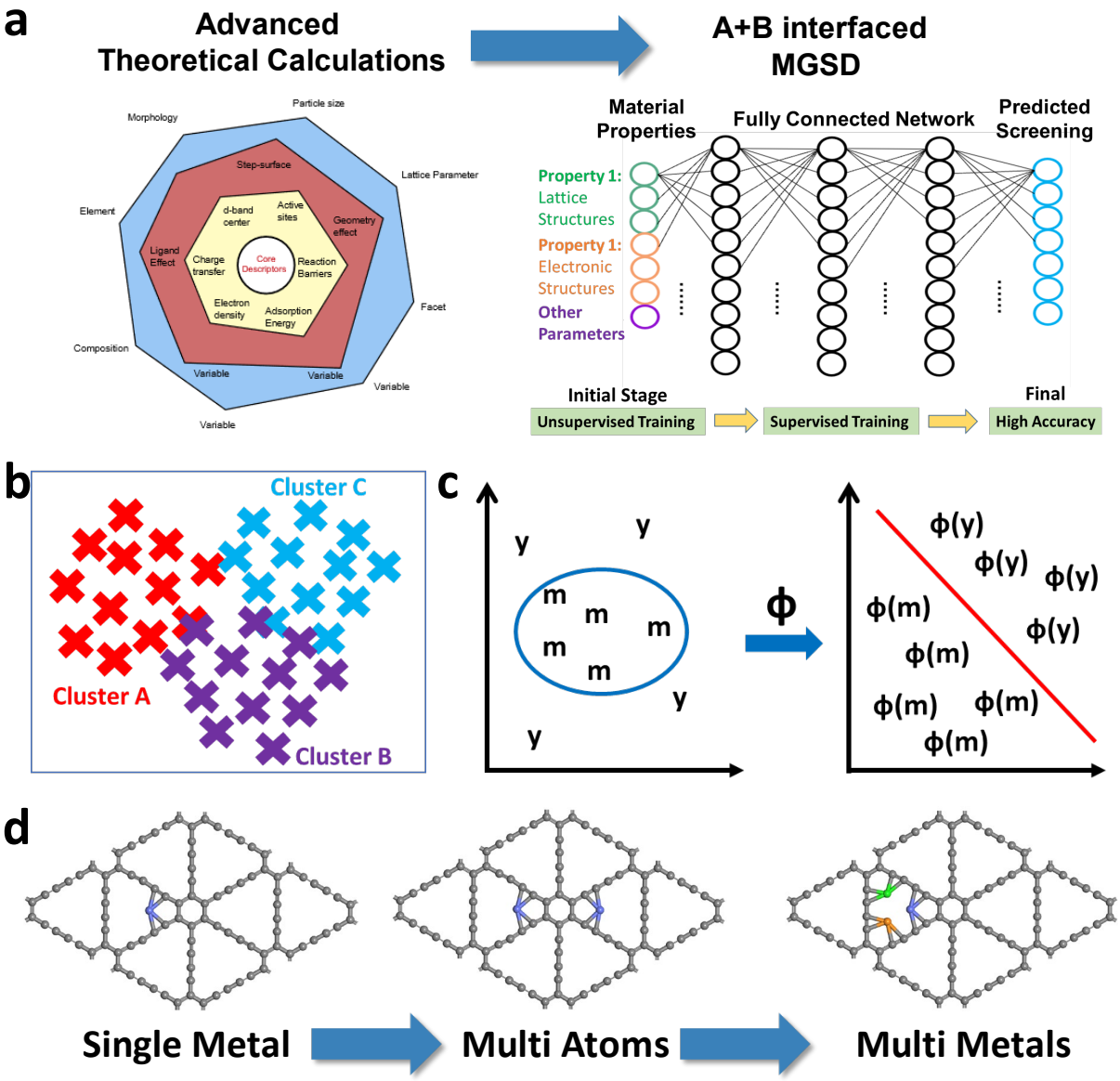

Figure 6. The future outlook for mapping strategy. (a) The further introduction of AI technology based deep-learning and big data (A+B) driven technologies for more complicated mapping strategy. Potential Algorithm for data mapping technologies. (b) Clustered data with overlapping data-points. (c) Demonstration of Kernel function for separating data. (d) Potential research directions of GDY-based multi-functional electrocatalysts.

Reference:

[1] M. Haruta; T. Kobayashi; H. Sano; N. Yamada, Novel Gold Catalysts for the Oxidation of Carbon Monoxide at a Temperature Far Below 0 C. *Chem Lett* **1987,** *16* (2), 405-408.
[2] G. A. Somorjai; J. Y. Park, Molecular Surface Chemistry by Metal Single Crystals and Nanoparticles from Vacuum to High Pressure. *Chem Soc Rev* **2008,** *37* (10), 2155-2162.
[3] M. Crespo-Quesada; A. Yarulin; M. Jin; Y. Xia; L. Kiwi-Minsker, Structure Sensitivity of Alkynol Hydrogenation on Shape-and Size-Controlled Palladium Nanocrystals: Which Sites Are Most Active and Selective? *J Am Chem Soc* **2011,** *133* (32), 12787-12794.
[4] G. G. Wildgoose; C. E. Banks; R. G. Compton, Metal Nanoparticles and Related Materials Supported on Carbon Nanotubes: Methods and Applications. *Small* **2006,** *2* (2), 182-193.
[5] L. Shang; T. Bian; B. Zhang; D. Zhang; L. Z. Wu; C. H. Tung; Y. Yin; T. Zhang, Graphene-Supported Ultrafine Metal Nanoparticles Encapsulated by Mesoporous Silica: Robust Catalysts for Oxidation and Reduction Reactions. *Angew Chem Int Ed* **2014,** *53* (1), 250-254.
[6] F. Yang; D. Deng; X. Pan; Q. Fu; X. Bao, Understanding Nano Effects in Catalysis. *National Science Review* **2015,** *2* (2), 183-201.
[7] B. Lim; M. Jiang; P. H. Camargo; E. C. Cho; J. Tao; X. Lu; Y. Zhu; Y. Xia, Pd-Pt Bimetallic Nanodendrites with High Activity for Oxygen Reduction. *science* **2009,** *324* (5932), 1302-1305.
[8] S. Guo; S. Sun, Fept Nanoparticles Assembled on Graphene as Enhanced Catalyst for Oxygen Reduction Reaction. *J Am Chem Soc* **2012,** *134* (5), 2492-2495.
[9] B. Qiao; A. Wang; X. Yang; L. F. Allard; Z. Jiang; Y. Cui; J. Liu; J. Li; T. Zhang, Single-Atom Catalysis of Co Oxidation Using Pt1/Feox. *Nat Chem* **2011,** *3* (8), 634-41.
[10] S. Yang; J. Kim; Y. J. Tak; A. Soon; H. Lee, Single-Atom Catalyst of Platinum Supported on Titanium Nitride for Selective Electrochemical Reactions. *Angew Chem Int Ed Engl* **2016,** *55* (6), 2058-62.
[11] J. P. Espinós; J. Morales; A. Barranco; A. Caballero; J. P. Holgado; A. R. González-Elipe, Interface Effects for Cu, Cuo, and Cu2o Deposited on Sio2 and Zro2. Xps Determination of the Valence State of Copper in Cu/Sio2 and Cu/Zro2 Catalysts. *The Journal of Physical Chemistry B* **2002,** *106* (27), 6921-6929.
[12] S. Wang; A. Y. Borisevich; S. N. Rashkeev; M. V. Glazoff; K. Sohlberg; S. J. Pennycook; S. T. Pantelides, Dopants Adsorbed as Single Atoms Prevent Degradation of Catalysts. *Nature Materials* **2004,** *3* (3), 143.
[13] B. Qiao; A. Wang; X. Yang; L. F. Allard; Z. Jiang; Y. Cui; J. Liu; J. Li; T. J. A. o. c. r. Zhang, Single-Atom Catalysis of Co Oxidation Using Pt 1/Feo X. *Nature chemistry* **2011,** *3* (8), 634.
[14] W. Tang; Z. P. Hu; M. J. Wang; G. D. Stucky; H. Metiu; E. W. McFarland, Methane Complete and Partial Oxidation Catalyzed by Pt-Doped Ceo2. *J Catal* **2010,** *273* (2), 125-137.
[15] W. Song; A. P. Jansen; E. J. Hensen, A Computational Study of the Influence of the Ceria Surface Termination on the Mechanism of Co Oxidation of Isolated Rh Atoms. *Faraday Discuss* **2013,** *162*, 281-92.
[16] V. Shapovalov; H. Metiu, Catalysis by Doped Oxides: Co Oxidation by Auxce1− Xo2. *J Catal* **2007,** *245* (1), 205-214.
[17] Z. P. Hu; H. Metiu, Effect of Dopants on the Energy of Oxygen-Vacancy Formation at the Surface of Ceria: Local or Global? *Journal of Physical Chemistry C* **2011,** *115* (36), 17898-17909.
[18] X. F. Yang; A. Wang; B. Qiao; J. Li; J. Liu; T. Zhang, Single-Atom Catalysts: A New Frontier in Heterogeneous Catalysis. *Acc Chem Res* **2013,** *46* (8), 1740-8.
[19] Z.-L. Wang; X.-F. Hao; Z. Jiang; X.-P. Sun; D. Xu; J. Wang; H.-X. Zhong; F.-L. Meng; X.-B. Zhang, C and N Hybrid Coordination Derived Co–C–N Complex as a Highly Efficient

Electrocatalyst for Hydrogen Evolution Reaction. *J Am Chem Soc* **2015,** *137* (48), 15070-15073.
[20] F. Li; G. F. Han; H. J. Noh; S. J. Kim; Y. L. Lu; H. Y. Jeong; Z. P. Fu; J. B. Baek, Boosting Oxygen Reduction Catalysis with Abundant Copper Single Atom Active Sites. *Energy & Environmental Science* **2018,** *11* (8), 2263-2269.
[21] Y. Xue; B. Huang; Y. Yi; Y. Guo; Z. Zuo; Y. Li; Z. Jia; H. Liu; Y. Li, Anchoring Zero Valence Single Atoms of Nickel and Iron on Graphdiyne for Hydrogen Evolution. *Nat Commun* **2018,** *9* (1), 1460.
[22] H. J. Qiu; Y. Ito; W. Cong; Y. Tan; P. Liu; A. Hirata; T. Fujita; Z. Tang; M. Chen, Nanoporous Graphene with Single-Atom Nickel Dopants: An Efficient and Stable Catalyst for Electrochemical Hydrogen Production. *Angew Chem Int Ed Engl* **2015,** *54* (47), 14031-5.
[23] H. Yu; Y. Xue; B. Huang; L. Hui; C. Zhang; Y. Fang; Y. Liu; Y. Zhao; Y. Li; H. Liu, Ultrathin Nanosheet of Graphdiyne-Supported Palladium Atom Catalyst for Efficient Hydrogen Production. *iScience* **2019,** *11*, 31-41.
[24] H. J. Qiu; Y. Ito; W. Cong; Y. Tan; P. Liu; A. Hirata; T. Fujita; Z. Tang; M. J. A. C. I. E. Chen, Nanoporous Graphene with Single-Atom Nickel Dopants: An Efficient and Stable Catalyst for Electrochemical Hydrogen Production. *Angew Chem Int Ed* **2015,** *54* (47), 14031-14035.
[25] M. Long; L. Tang; D. Wang; Y. Li; Z. Shuai, Electronic Structure and Carrier Mobility in Graphdiyne Sheet and Nanoribbons: Theoretical Predictions. *ACS nano* **2011,** *5* (4), 2593-2600.
[26] Y. Zhao; J. Wan; H. Yao; L. Zhang; K. Lin; L. Wang; N. Yang; D. Liu; L. Song; J. Zhu; L. Gu; L. Liu; H. Zhao; Y. Li; D. Wang, Few-Layer Graphdiyne Doped with Sp-Hybridized Nitrogen Atoms at Acetylenic Sites for Oxygen Reduction Electrocatalysis. *Nat Chem* **2018,** *10* (9), 924-931.
[27] M. Li; Z.-K. Wang; T. Kang; Y. Yang; X. Gao; C.-S. Hsu; Y. Li; L.-S. Liao, Graphdiyne-Modified Cross-Linkable Fullerene as an Efficient Electron-Transporting Layer in Organometal Halide Perovskite Solar Cells. *Nano Energy* **2018,** *43*, 47-54.
[28] J. Deng; H. Li; J. Xiao; Y. Tu; D. Deng; H. Yang; H. Tian; J. Li; P. Ren; X. Bao, Triggering the Electrocatalytic Hydrogen Evolution Activity of the Inert Two-Dimensional Mos 2 Surface Via Single-Atom Metal Doping. *Energy Environmental Science* **2015,** *8* (5), 1594-1601.
[29] H. Yu; Y. Xue; B. Huang; L. Hui; C. Zhang; Y. Fang; Y. Liu; Y. Zhao; Y. Li; H. Liu; Y. Li, Ultrathin Nanosheet of Graphdiyne-Supported Palladium Atom Catalyst for Efficient Hydrogen Production. *iScience* **2019,** *11*, 31-41.
[30] K. W. Lux; E. J. Cairns, Lanthanide–Platinum Intermetallic Compounds as Anode Electrocatalysts for Direct Ethanol Pem Fuel Cells. *J Electrochem Soc* **2006,** *153* (6), A1132.
[31] Z. Tang; G. Lu, High Performance Rare Earth Oxides Lnox (Ln=Sc, Y, La, Ce, Pr and Nd) Modified Pt/C Electrocatalysts for Methanol Electrooxidation. *J Power Sources* **2006,** *162* (2), 1067-1072.
[32] J. Xu; T. Liu; J. Li; B. Li; Y. Liu; B. Zhang; D. Xiong; I. Amorim; W. Li; L. Liu, Boosting the Hydrogen Evolution Performance of Ruthenium Clusters through Synergistic Coupling with Cobalt Phosphide. *Energy & Environmental Science* **2018,** *11* (7), 1819-1827.
[33] J. N. Tiwari; S. Sultan; C. W. Myung; T. Yoon; N. Li; M. Ha; A. M. Harzandi; H. J. Park; D. Y. Kim; S. S. Chandrasekaran; W. G. Lee; V. Vij; H. Kang; T. J. Shin; H. S. Shin; G. Lee; Z. Lee; K. S. Kim, Multicomponent Electrocatalyst with Ultralow Pt Loading and High Hydrogen Evolution Activity. *Nature Energy* **2018,** *3* (9), 773-782.
[34] W. Chen; J. Pei; C. T. He; J. Wan; H. Ren; Y. Zhu; Y. Wang; J. Dong; S. Tian; W. C. Cheong; S. Lu; L. Zheng; X. Zheng; W. Yan; Z. Zhuang; C. Chen; Q. Peng; D. Wang; Y. Li,

Rational Design of Single Molybdenum Atoms Anchored on N-Doped Carbon for Effective Hydrogen Evolution Reaction. *Angew Chem Int Ed Engl* **2017,** *56* (50), 16086-16090.
[35] H. Fei; J. Dong; M. J. Arellano-Jimenez; G. Ye; N. Dong Kim; E. L. Samuel; Z. Peng; Z. Zhu; F. Qin; J. Bao; M. J. Yacaman; P. M. Ajayan; D. Chen; J. M. Tour, Atomic Cobalt on Nitrogen-Doped Graphene for Hydrogen Generation. *Nat Commun* **2015,** *6*, 8668.
[36] S. Kiyohara; T. Miyata; K. Tsuda; T. Mizoguchi, Data-Driven Approach for the Prediction and Interpretation of Core-Electron Loss Spectroscopy. *Sci Rep* **2018,** *8* (1), 13548.
[37] E. Kim; K. Huang; A. Saunders; A. McCallum; G. Ceder; E. Olivetti, Materials Synthesis Insights from Scientific Literature Via Text Extraction and Machine Learning. *Chem Mater* **2017,** *29* (21), 9436-9444.
[38] K. T. Butler; D. W. Davies; H. Cartwright; O. Isayev; A. Walsh, Machine Learning for Molecular and Materials Science. *Nature* **2018,** *559* (7715), 547-555.
[39] M. H. S. Segler; M. Preuss; M. P. Waller, Planning Chemical Syntheses with Deep Neural Networks and Symbolic Ai. *Nature* **2018,** *555* (7698), 604-610.
[40] M. Popova; O. Isayev; A. Tropsha, Deep Reinforcement Learning for De Novo Drug Design. *Sci Adv* **2018,** *4* (7), eaap7885.
[41] J. R. Kitchin, Machine Learning in Catalysis. *Nature Catalysis* **2018,** *1* (4), 230-232.
[42] Q. Zhou; P. Tang; S. Liu; J. Pan; Q. Yan; S. C. Zhang, Learning Atoms for Materials Discovery. *Proc Natl Acad Sci U S A* **2018,** *115* (28), E6411-E6417.
[43] A. W. Dougherty; J. You, A Kernel-Based Adaptive Fuzzy C-Means Algorithm for M-Fish Image Segmentation. **2017**, 198-205.

TOC

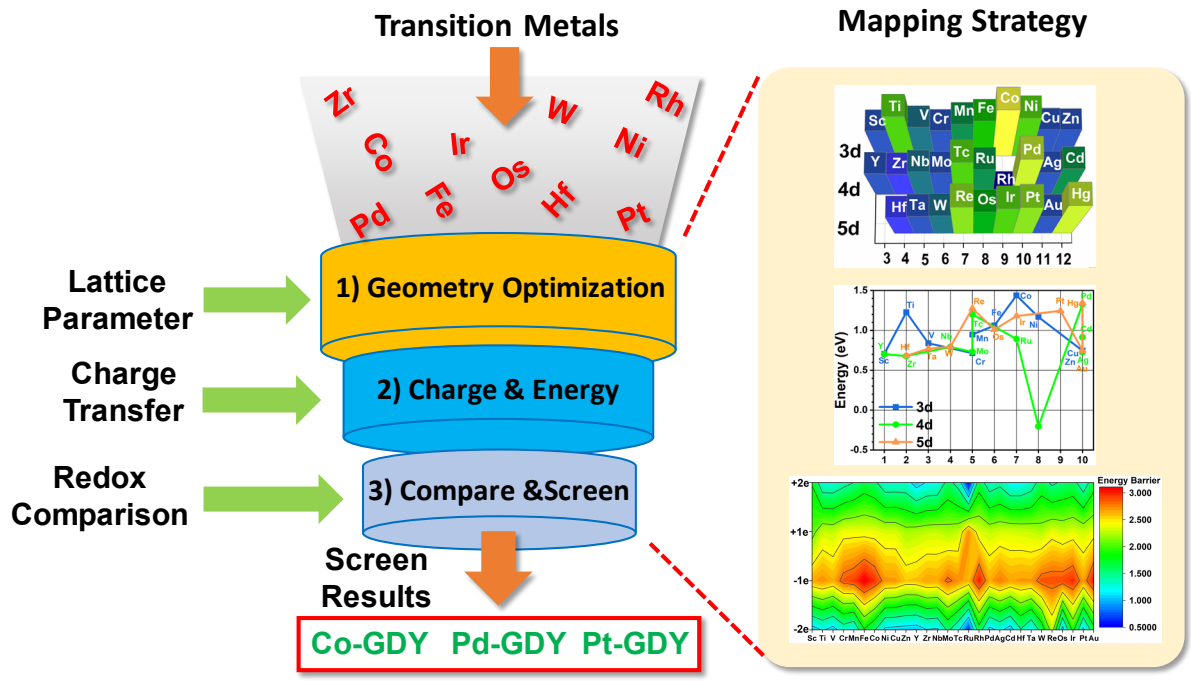

Synopsis

Illustration of the mapping strategy for screening AC candidates.